Landslides manuscript No.
(will be inserted by the editor)

Estimation of dynamic friction and movement history of large landslides

Masumi Yamada · Anne Mangeney · Yuki Matsushi · Takanori Matsuzawa

Received: date / Accepted: date

Abstract We performed seismic waveform inversions and numerical landslide simulations of deep-seated landslides in Japan to understand the dynamic evolution of friction of the landslides. By comparing the forces obtained from a numerical simulation to those resolved from seismic waveform inversion, the coefficient of friction during sliding was well constrained between 0.3 and 0.4 for landslides with volumes of 2-8$\times 10^6$ m^3. We obtained similar coefficients of friction for landslides with similar scale and geology, and they are consistent with the empirical relationship between the volume and dynamic coefficient of friction obtained from the past studies. This hybrid method of the numerical

M. Yamada
Disaster Prevention Research Institute, Kyoto University, Uji, Gokasho, 611-0011, Japan
Tel.: +81-774-38-4020
Fax: +81-774-38-4215
E-mail: masumi@eqh.dpri.kyoto-u.ac.jp

A. Mangeney
Institut de Physique du Globe de Paris, Paris, Sorbonne Paris Cité, Université Paris Diderot, UMR 7154 CNRS, Paris, France

Y. Matsushi
Disaster Prevention Research Institute, Kyoto University, Uji, Gokasho, 611-0011, Japan

T. Matsuzawa
National Research Institute for Earth Science and Disaster Prevention, 3-1, Tennodai, Tsukuba, Ibaraki, 305-0006, Japan

simulation and seismic waveform inversion shows the possibility of reproducing or predicting the movement of a large-scale landslide. Our numerical simulation allows us to estimate the velocity distribution for each time step. The maximum velocity at the center of mass is 12-36 m/s and is proportional to the square root of the elevation change at the center of mass of the landslide body, which suggests that they can be estimated from the initial DEMs. About 20% of the total potential energy is transferred to the kinetic energy in our volume range. The combination of the seismic waveform inversion and the numerical simulation helps to obtain the well-constrained dynamic coefficients of friction and velocity distribution during sliding, which will be used in numerical models to estimate the hazard of potential landslides.

Keywords landslide · dynamic friction · numerical simulation · seismic waveform inversion · force history

1 Introduction

Dynamic friction of landslides is one of the key factors controlling the mobility of slope failures. The runout distance and velocity of landslides strongly depend on this parameter. Various friction models calibrated by analytical solutions on the laboratory scale and runout distance of landslides have been proposed (e.g. Guthrie et al. 2012; Moretti et al. 2012; Lucas et al. 2014; Pastor et al. 2014).

Conventionally, it was estimated by the ratio of the drop height (H) and runout (L), which is referred as Heim's ratio (H/L). Several observations based on experimental and field surveys indicate that larger landslides have a smaller apparent coefficient of friction (Hsü 1975; Dade and Huppert 1998; Legros 2002; Balmforth and Kerswell 2005; Mangeney et al. 2010; Farin et al. 2014). Lucas et al. (2014) proposed an empirical velocity-weakening friction law calibrated by the extension of landslide deposits using the SHALTOP numerical model. The results showed that the effective friction coefficient (a function of the slope, thickness of the released mass, and distance travelled by the front along the slope) explained the volume dependency more precisely than Heim's ratio. The advantage of numerical simulations is that three dimensional topography and mass deformation can be included, so the results can be more realistic than those using the more straightforward Heim's ratio.

Recent studies show that the use of seismic signals allows us to obtain the physical parameters of high-speed landslides, such as the time history of the force acting on the surface, velocity, coefficient of friction (e.g. Kawakatsu 1989; Brodsky et al. 2003; Favreau et al. 2010; Moretti et al. 2012; Yamada et al. 2013; Allstadt 2013; Ekström and Stark 2013; Moretti et al. 2015). It is a novel approach to estimate dynamic parameters of landslides, which may be difficult to obtain from a conventional field survey after the occurrence of a disaster. Yamada et al. (2016) used the SHALTOP numerical model and seismic waveform inversion to resolve the time-evolution of friction. They obtained a well constrained average coefficient of friction over the volume for the 2011 Akatani landslide. This event was one of the sequential landslides caused by a typhoon, so it is important to study these landslides in similar geology and condition to understand the general dynamic behavior of landslides. Investigating the behavior of gravitational flows in a similar environment makes it possible to get insight into the possible volume dependence on the coefficient of friction.

In this paper, we used the seismic data of four large-scale deep-seated landslides in Japan caused by typhoons to estimate the dynamic frictional coefficients during the movement (see Table 1). In general, the seismic signals due to the landslides are much weaker than earthquakes, so they are generally difficult to detect with global or regional broadband seismic networks unless the landslides are greater than 10^7 m^3 in volume (Ekström and Stark 2013). Here, we utilise a very dense array of high-sensitivity accelerometers installed in boreholes across Japan (Okada et al. 2004). The sensors are collocated with Hi-net (High sensitivity seismograph network, Japan) and the average spacing of the stations is 20-25 km. Another advantage of these landslides is the precise topographic data obtained before and after the events from LiDAR data and photogrammetry, which enable direct measurements of the potential energy released by the landslide and provide a digital elevation model (DEM) for the numerical simulations. Using the method of Yamada et al. (2016), we propose a friction model, which describes the movement of these large bedrock landslides. The well-constrained dynamic coefficients of friction and velocity distribution during sliding will be used for the numerical model to assess the hazard of future potential landslides.

2 Sites and data

We focused on large landslides caused by heavy rainfall which occurred after 2004, when the dense seismic networks were installed in Japan (Okada et al. 2004; Public Works Research Institute, Japan 2017). Here we selected four large-scale deep-seated landslides in the south-western outer arc of Japan: one in Kyushu island: Nonoo, and three in the Kii Peninsula: Akatani, Iya, and Nagatono. The Nonoo landslide occurred on September 6, 2005 when Typhoon Nabi (No. 14 in Japan) produced heavy rainfall; over 500 mm during 72 hours on the Kyushu area. The Akatani, Iya and Nagatono landslides occurred on September 4, 2011, when Typhoon Talas (No. 12 in Japan) supplied rainfall ranging 1000 to 2000 mm over five days on the Kii Peninsula. We also checked the seismic data of all other large landslides greater than 1 $\times 10^6$ m^3 since 2004, but the signal-to-noise ratio was not high enough to detect and reconstruct the motion of landsliding. Landslides right after large earthquakes are not suitable for this analysis either since the signal is contaminated by the earthquakes strong motion.

The locations and other information of the landslides are shown in Table 1 and Figure 1. The failed slopes have geometries of 460 to 1100 m in horizontal length and 270 to 640 m in vertical relief, with sliding volumes 2-8 $\times 10^6$ m^3. The geology of all the landslides are underlain by Neogene to Cretaceous accretionary sedimentary rocks. The bedrock of the Nonoo landslide is alternating beds of sandstone and mudstone, which have a north-ward inclination around 30 degrees and a NE-SW strike parallel to the dip direction of the sliding hillslope (Chigira 2009). Landslides in the Kii area all occurred on dipping slopes of sandstone-mudstone alternating beds or chaotic rocks; for Akatani and Nagatono, a set of high-angle faults forms a wedge structure in the strata, which may bound the side scars of the landslides (Chigira et al. 2013). Slope angles for Akatani and Nagatono are 34 and 33 degrees respectively, whereas that of Iya is slightly lower, 24 degrees.

We used the F-net broadband seismograms and high-sensitivity accelerograms recorded in boreholes across Japan (Okada et al. 2004). F-net contains three component STS-2 sensors with average spacing of about 100 km. The high-sensitivity accelerometers are collocated with the Hi-net velocity seismometers and consist of two horizontal components. The average spacing of the stations is 20-25 km. Since seismic signals due to landslides are very weak, the seismic station must be close to the landslide. We checked all stations less than 100 km from the landslides, and did not use records with poor signal-to-noise ratio. We mainly used data recorded at distances less than 50 km from the landslides (see Figure 2).

We obtained a DEM with 1 m grid spacing before and after the landslide from airborne LiDAR data (Yamada et al. 2013). If the LiDAR data before the landslide was not available, a 10m DEM made by photogrammetry was used instead (Geospatial Information Authority of Japan 2017) (see Table 1). The domain of the numerical simulation is shown in Figure 1. Due to the limitation of computation memory, we downsampled (or resampled for the 10m DEM) the DEM to a 4 m grid for the Nonoo landslide, and a 5 m grid for the other landslides. We used finer grids for the Nonoo landslide since it is smaller than others, but the long period waves greater than 10 s (wavelength of a few kilometers) used in this study are insensitive to this size of grid. We prepared two topographic data sets from the DEM; the sliding surface and the mass thickness on the surface. The sliding surface was constructed by taking the lower values of the DEMs before and after the landslide. The thickness of the sliding mass was computed by subtracting this sliding surface from the DEM before the landslide.

3 Methods

In order to explore the dynamic friction of the large landslides, we performed seismic waveform inversions and numerical simulations with our DEMs. The seismic waveform inversion provides a single force at the landslide which generates the seismic waveforms (Nakano et al. 2008). The numerical simulation allows us to compute the force acting on the sliding surface, which is the summation of the stress field applied by the landslide mass (Bouchut et al. 2003; Mangeney et al. 2000).

These force histories are strongly controlled by the flow rheology, i.e., dynamic friction. Therefore, we can modulate the behavior of the sliding mass by changing the friction model. By comparing these forces with those calculated from the seismic waveform inversion in the same frequency range, we can identify a friction model which describes the movements of large bedrock landslides (Moretti et al. 2015; Yamada et al. 2016). Note that the result of

Akatani landslide was presented in Yamada et al. (2016) and we use their results to compare with the other landslides investigated here.

3.1 Seismic Waveform Inversion

We performed a waveform inversion using broadband seismic records and high-sensitivity accelerograms to obtain the source time function. We processed these records according to the following procedure. First, we removed the mean from the time series and corrected for the instrumental response in all waveforms. A non-causal fourth order Butterworth filter was applied to remove noise. We tuned the corner frequencies of the filter for each event shown in Table 2 to maximize the signal-to-noise ratio. The data was integrated in the time domain to obtain the displacement component. We then downsampled the data to reduce the sampling frequency to 1 Hz. We used these filtered displacement records for the inversion.

Following the method of Nakano et al. (2008), we performed a waveform inversion in the frequency domain to determine the source process of the landslide. We calculated Green's functions at the given location of the landslide, using a discrete wavenumber method (Bouchon 1979) and the Japan Meteorological Agency (JMA) one-dimensional velocity structure model (Ueno et al. 2002). Assuming a single-force mechanism for the landslide source (Hasegawa and Kanamori 1987), we estimated the least-squares solution in the frequency domain. We performed an inverse Fourier transform on the solution to determine source time functions for three single-force components at each source location (Nakano et al. 2008).

3.2 Shaltop Numerical Simulation

We used the SHALTOP numerical model to compute the spatiotemporal stress field applied to the sliding surface by the moving landslide mass. It is based on the thin-layer approximation and depth-averaging of the Navier-Stokes equations without viscosity (Bouchut et al. 2003; Mangeney et al. 2000; Mangeney-Castelnau et al. 2005). The behavior of the sliding mass is strongly controlled by the friction model. Followed by Yamada et al. (2016), we tested two different friction laws: Coulomb friction, in which the dynamic coefficient of friction is independent of sliding velocity, and a velocity-dependent friction model (Pouliquen and Forterre 2002; Jop et al. 2006; Liu et al. 2016).

The velocity-dependent friction model is defined by the following equation:

$$\mu = \frac{\mu_o - \mu_w}{1 + ||U||/U_w} + \mu_w \tag{1}$$

where μ_o is the static coefficient of friction, μ_w is the dynamic coefficient of friction during sliding, and U_w is the characteristic velocity for the onset of weakening. $||U||$ is the scalar amplitude of the three component velocity vector at each grid cell. Note that μ_o is the coefficient of friction when $||U|| = 0$, μ_w is the coefficient of friction when $||U|| = \infty$, and U_w controls how quickly the coefficient of friction drops as a function of velocity. We computed μ for each grid cell at each time step.

3.3 Estimation of Coefficients of Friction

We evaluated different friction models by comparing the simulated force with that obtained from seismic waveform inversion. The most probable coefficients for the friction model were obtained by a grid search. A parameter range for the Coulomb friction model (μ_{const}) is between 0.2 and 0.5 with a 0.02 increment. We selected this range so that the local minima are included. A three dimensional (3D) grid search for the velocity dependent friction model was performed in the following parameter space: $\mu_o = (0.10, 0.20, 0.22, 0.24, ..., 0.36, 0.38, 0.40)$, $\mu_w = (0.1, 0.2, 0.3, 0.4)$, and $U_w = (0.5, 1, 2, 3, 4)$ m/s.

The normalized residual (hereafter referred to as the residual), defined as the following, is used to evaluate the quality of the fit:

$$R = \frac{\sum_{t=1}^{nt}(f_o(t) - f_s(t - \Delta t))^2}{\sum_{t=1}^{nt}(f_o(t))^2} \tag{2}$$

where $f_o(t)$ and $f_s(t)$ are the force at time t computed from the seismic waveform inversion and numerical simulation, respectively, and nt is the total duration of the force in 1 s intervals. Δt is selected to minimize the mean of the residuals for the three-component forces.

4 Results

4.1 Seismic Waveform Inversion

Figure 3 shows the source time functions of three single force components obtained from the seismic waveform inversion. Waveform fittings between observed and synthesized seismograms are shown in Supplemental Figures S1-S3.

We have better residuals for the Iya and Nonoo landslides than the Nagatono landslide, even though we used a wider frequency range for those landslides (see Table 2). This is because they are larger landslides and have closer seismic stations, which results in a better signal-to-noise ratio for the data. The waveform inversion results of the Akatani landslide were presented in Yamada et al. (2013), with a normalized residual (equation 2) of 0.08.

Figure 3 shows that phases of all three components are synchronized and the direction of the peak amplitude is the same as the landslide movement direction. This suggests that the force history obtained by the seismic waveform inversion reflects the main landslide movement. Note that the information for the vertical direction is limited since the high-sensitivity accelerometer consists of two horizontal components only. Therefore, we may not have enough resolution for the vertical component. For example, the force in the UD (up-down) component in Figure 3(c) is clearly overestimated, as we can see the poor fit in the UD displacement at TMC station (Supplemental Figure S3). For the Iya and Nonoo landslides, we used only EW (east-west) and NS (north-sourth) components to compute the residual in equation 2. We selected EW and UD components for the Nagatono landslide since they have better signal-to-noise ratio.

4.2 Estimation of Coefficients of Friction

Figure 4 shows the residual of the coefficients of the Coulomb friction model. The parameter space is reasonably smooth, and the most probable coefficient of friction (μ_{const}) is 0.32 for Iya, 0.40 for Nagatono, and 0.36 for Nonoo. The μ_{const} of Akatani landslide in Yamada et al. (2016) was 0.3, so these are slightly larger than that of the Akatani landslide. The coefficients may vary slightly depending on the filter type, components, or stations, but it would be difficult to change the values of the most probable coefficients by 0.1.

Figure 5 shows the residual of the velocity dependent friction model in the 3D parameter space. The optimal parameter sets are (μ_o, μ_w, U_w) =(0.6, 0.24, 4) for Akatani, (0.7, 0.28, 0.5) for Iya, (0.7, 0.34, 3) for Nagatono, and (0.7, 0.2, 4) for Nonoo. Although μ_w is theoretically the smallest coefficient of friction in the model, the coefficient of friction during sliding is controlled by both U_w and μ_w. In an extreme case, if $U_w = \infty$, the coefficient of friction does not depend on μ_w.

In order to evaluate the coefficient of friction during sliding, time history of the mass-weighted average of the coefficient of friction for each model in Figure 5 is shown in Figure 6. Although the velocity dependent model has a trade-off between parameters in Figure 5, the average coefficient of friction during sliding seems to be well constrained with a small variance. To evaluate the variation of the dynamic coefficient of friction, the minimum coefficient of friction for each model was computed, and the models whose residual was within 0.05 from the smallest residual were selected. The mean and standard deviation for the selected models are shown in Figure 7(a). The standard deviation of the minimum coefficient of friction is less than 0.03, which suggests that the dynamic coefficient of friction is well constrained, even though the standard deviation of μ_w seems to be large in Figure 5.

4.3 Deposit of landslides

Figure 8 shows the comparison between actual extent of the valley-fill deposits and the results of numerical simulations for the four landslides. Note that the depositional areas were estimated from elevation difference of the DEMs before and after the event; hence the upstream side of the deposits includes the areas of the barrier lakes in the cases of Akatani, Nagatono, and Iya (Figures 8(a), (b), and (c)). For the Nonoo case, since the landslide dam had been breached just after the event, the toe of the deposit was eroded by the outburst of the lake water. Low precision of the DEM before the landslide in the Iya and Nonoo cases made from aerial photogrammetry also resulted in the larger uncertainty in the reconstruction of deposit thickness.

Although the horizontal extent of deposits seems to be largely consistent, there are discrepancies in the distributions of thickness. One of the main reasons for this discrepancy is the limitation of the friction model. We used a model with a velocity-weakening friction law, as the friction decreases along with the sliding and then increases to the static value at the end of sliding when the velocity decreases. This hypothesized process has been developed for the modeling of dry granular flows. However, in reality, the pressure of the pore fluid significantly changes the landslide dynamics (Iverson 1997; Schulz et al. 2009). Especially when the sliding mass reaches the valley bottom, generation of high pore-water pressure due to the mass compression alters the behavior of the mass settlement. Indeed, parts of the landslide material fluidized and ran out as a debris flow down the valley.

Another limitation of the depth-averaged models is that the whole column stops at the same time, whereas in actual granular flows there may be a propagation of the static/flowing interface towards the surface during the arrest phase (Ionescu et al. 2015; Fernández-Nieto et al. 2016). This could also change the final distribution of thicknesses.

The mass change due to erosion and entrainment at the bottom of sliding is another cause to produce this discrepancy of deposits. The erosional processes may significantly change the distribution of the deposit, which can be demonstrated by the change of the mass during sliding (Moretti et al. 2012). This entrainment effect was not considered in the model used here because of the relatively short runout distance.

As we have seen in past landslides, the dominant long-period seismic signal was effectively generated during the beginning to middle stages of the landslide movement when the whole mass moves uniformly (Yamada et al. 2013; Hibert et al. 2015, 2017). The friction model is calibrated by the seismic signal and strongly depends on the large amplitudes during the early stage of the landslide. So it is difficult to reproduce the later extent of the deposit, because the model is strongly dependent on the earlier long-period seismic signals.

5 Discussion

We obtained a force history of large landslides from the seismic waveform inversion with broadband and high-sensitivity accelerometer data, which reflects the movement of the landslides. The numerical simulation benchmarked by the force history provides a reasonable estimate of the dynamic coefficient of friction.

5.1 Volume vs Coefficients of Friction

Figure 7(a) shows the relationship between the volume and coefficient of friction for the Coulomb and velocity dependent friction model of four landslides in this study. The coefficient of friction is well constrained between 0.3 and 0.4, although the range of the volume is limited possibly due to the similar geology (accretionary sedimentary rocks) and geometry (hillslope angle of $30° \pm 6°$). These landslides in the same environment with similar volumes seem to have a comparable coefficient of friction estimated by the method of coupled seismic and modelling analysis. The Akatani landslide in Figure 7(a) shows little difference between the Coulomb friction model and velocity dependent friction model, which indicates the dynamic coefficient of friction is mostly constant during sliding, and can be approximated by the Coulomb friction model.

Figure 7(b) compares the relationship between the volume of the landslides from other studies and coefficients of friction obtained by: (1) the numerical simulation benchmarked by the deposits (Kuo et al. 2009; Tang et al. 2009; Kuo et al. 2011; Lucas et al. 2014), (2) the numerical simulation benchmarked by the seismic signals (Moretti et al. 2015, this study), and (3) the force history of seismic waveform inversion (Brodsky et al. 2003; Allstadt 2013; Yamada et al. 2013). Smaller, rockfall-type landslides (Volume 10^2-10^3 m^3) show a coefficient of friction of 0.6-0.7, whereas larger, deep-seated landslides (Volume $> 10^7$ m^3) show a coefficient of friction smaller than 0.3. This is consistent with past observations based on field surveys, which show that the larger landslides tend to have a smaller apparent coefficient of friction (Scheidegger 1973; Hsü 1975; Dade and Huppert 1998).

We obtained similar coefficients of friction for the landslides with similar scale and geology. They are consistent with the empirical relationship between the volume and dynamic coefficient of friction obtained from past studies. This hybrid method of the numerical simulation and seismic waveform inversion shows the possibility of reproducing or predicting the movement of a large-scale landslide. However, direct observations of landslide movement, such as velocity, are required to verify these dynamic parameters.

5.2 Velocity history and Energy partition

Figure 9 shows the velocity history at the center of mass for the most probable velocity dependent friction model. The Akatani landslide shows the largest velocity with 35.4 m/s, but other landslides also show a velocity greater than 10 m/s. Although the maximum velocity and duration vary depending on the landslides, the macroscopic behavior, acceleration and deceleration phases, are similar for all landslides. As discussed in Yamada et al. (2013), the acceleration phase represents the movement of the mass down the slope, and the deceleration phase represents the stopping of the mass at the bottom of the slope. This acceleration/deceleration waveform is typical in simple decreasing slope topography such as V-shaped valleys made by erosion (e.g. Yamada et al. 2013; Hibert et al. 2015). More complex topography generates more fluctuating velocities (e.g. Schneider et al. 2010; Moretti et al. 2012; Allstadt 2013).

One of the advantages of this hybrid approach is to obtain the transition of the potential and kinetic energies directly from deposit and velocity snapshots. Landslide motion involves a cascade of energy that begins with gravitational potential energy transferred to kinetic energy, and eventually, all energy will be dissipated by the heat energy and fracture energy caused by grain contact friction and inelastic collisions (Iverson 1997). This energy transition depends significantly on the natural topography and materials (rock type and fluid), so estimating the movement of a landslide in advance has difficulty even if we know the precise topography of the slope.

Figure 10 shows the relationship between the elevation change of the DEM (h) and maximum velocity (v) at the center of mass estimated from our numerical simulations. It shows the linear relationship for this volume range, with $v = 2\sqrt{h} = 0.45 \times \sqrt{2gh}$. Ekström and Stark (2013) also provide these parameters obtained from the seismic waveform inversions and show the consistent relationship with our dataset (Figure 10). The elevation change at the center of mass is relatively available from DEM even before the landslide so the maximum velocity can be estimated from this relationship. It also suggests the ratio of potential energy transferred to the kinetic energy is about constant, even if the size of the landslide is different. Suppose the total potential energy is converted to the kinetic energy under unrealistic conditions, we obtain $v = \sqrt{2gh}$. For our empirical relationship, about 20% (=0.45^2) of the potential energy was converted to the kinetic energy. Our analysis provides the relationship between kinetic energy and the potential energy empirically for future landslide hazard analysis.

5.3 Limitations and Potential Applications for Hazard Analysis

Here we summarize the potential causes of uncertainties of this approach to estimate the dynamic coefficient of friction. First of all, the accuracy of the DEM is important. The DEM created by the photogrammetry had poor resolution and caused uncertainty in the deposit distribution of Figures 8(b) and (d). If the mass of the landslide before sliding and the deposits of the landslide after sliding overlap, the sliding surface cannot be obtained by the DEMs, and that causes an error of about 10% in the volume estimation.

A large long-period seismic signal was produced at the beginning to middle stage of landslide movement, and a short-period seismic signal was dominant at the end of sliding. Therefore, the calibration by the seismic signal strongly depends on the early stage of the landslide. The coefficient of friction during the main sliding is relatively well calibrated, but the friction at the end of the landslide, when the effect of excess pore pressure are significant, has poor resolution. This effect and lack of key physical processes in the numerical models (fragmentation, erosion, presence of fluids, etc.) may explain why the extent of the deposit is difficult to reproduce by our friction law.

Despite the limitations, this empirical friction law can provide useful insights for future landslide hazard analysis. The movement of a landslide can be computed by the SHALTOP numerical model, once the topography of hillslopes and mass distribution are obtained. The horizontal extent of the potential area of future landslides can be obtained from the geomorphic interpretation for signals of deep-seated gravitational deformation of bedrock appearing on the ground surface using a high-resolution digital topographic model (Chigira et al. 2013). The thickness of the unstable mass can be estimated by the empirical relationship between the surface area and depth of the past landslides. The simulation can also be calibrated by the relationship between the elevation change of the deposit and maximum velocity at the center of mass in this study. The numerical simulation provides a reliable velocity of a landslide since the force acting on the sliding surface is calibrated by seismic records, however, mass fragmentation, erosion, and pore water, should be carefully examined to better estimate the extent of the runout.

6 Conclusions

We performed seismic waveform inversions and numerical landslide simulations of deep-seated landslides in Japan to understand the dynamic evolution of friction of the landslides. By comparing the forces obtained from numerical simulation to those resolved from seismic waveform inversion, the coefficient of friction during sliding was well constrained between 0.3 and 0.4 for landslides with volume of 2-8$\times10^6$ m^3.

We obtained similar coefficients of friction for landslides with similar scale and geology. They are consistent with the empirical relationship between the volume and dynamic coefficient of friction obtained from past studies. This hybrid method of the numerical simulation and seismic waveform inversion shows the possibility of reproducing or predicting the movement of a large-scale landslide.

Our numerical simulations allow us to estimate the velocity distribution at each time step. The maximum velocity at the center of mass shows a linear relationship with the square root of the elevation change at the center of mass, which suggests that they can be estimated from the initial DEMs. About 20% of the total potential energy is transferred to the kinetic energy in our volume range.

The combination of the seismic waveform inversion and the numerical simulation helps to obtain the well-constrained dynamic coefficients of friction and velocity distribution during sliding, which will be used for the numerical model to estimate the hazard of potential landslides.

Table 1 Landslide properties.

Name	Time (JST)	Vol. (m^3)	L (m)	H (m)	L_{CM} (m)	H_{CM} (m)	Slope	DEM
Akatani	16:23, 9/4, 2011	7.38×10^6	1100	640	514	265	34°	1m/1m
Iya	06:54, 9/4, 2011	4.67×10^6	610	300	217	76	24°	10m/1m
Nagatono	10:45, 9/4, 2011	3.63×10^6	610	400	281	144	33°	1m/1m
Nonoo	21:49, 9/6, 2005	2.72×10^6	460	270	138	65	31°	10m/1m

The indices are: occurrence time, volume, horizontal hillslope length, vertical hillslope relief, horizontal displacement at the center of mass, elevation change at the center of mass, average slope angle, and resolution of DEM (before/after), from the left.

Table 2 Simulation results.

Name	Waveform inversion		Numerical simulation			
	Freq. (Hz)	Force (N)	μ_{const}	$\bar{\mu}_{dyn}$	(μ_o, μ_w, U_w)	Vel. (m/s)
Akatani	0.01-0.1	$5.22*10^{10}$	0.30	0.30	(0.6,0.24,4)	35.5
Iya	0.016-0.1	$1.09*10^{10}$	0.32	0.30	(0.7,0.28,0.5)	12.2
Nagatono	0.02-0.1	$1.65*10^{10}$	0.40	0.39	(0.7,0.34,3)	21.2
Nonoo	0.01-0.1	$1.23*10^{10}$	0.36	0.32	(0.7,0.20,4)	13.6

The indices are: frequency range for the waveform inversion, maximum force in the vector sum estimated from the waveform inversion, the best coefficient of friction for Coulomb friction model, the mean dynamic coefficient of friction for the velocity dependent friction model, parameters for the velocity dependent friction model, and maximum velocity at the gravity center, from the left.

References

Allstadt, K. (2013). Extracting source characteristics and dynamics of the august 2010 mount meager landslide from broadband seismograms. *Journal of Geophysical Research: Earth Surface*, 118(3):1472–1490.

Balmforth, N. and Kerswell, R. (2005). Granular collapse in two dimensions. *Journal of fluid mechanics*, 538:399–428.

Bouchon, M. (1979). Discrete wave number representation of elastic wave fields in three-space dimensions. *Journal of Geophysical Research*, 84(B7):3609–3614.

Bouchut, F., Mangeney-Castelnau, A., Perthame, B., and Vilotte, J.-P. (2003). A new model of Saint Venant and Savage-Hutter type for gravity driven shallow water flows. *Comptes rendus mathematique*, 336(6):531–536.

Brodsky, E., Gordeev, E., and Kanamori, H. (2003). Landslide basal friction as measured by seismic waves. *Geophysical Research Letters*, 30(24):2236.

Chigira, M. (2009). September 2005 rain-induced catastrophic rockslides on slopes affected by deep-seated gravitational deformations, kyushu, southern japan. *Engineering Geology*, 108(1):1–15.

Chigira, M., Tsou, C.-Y., Matsushi, Y., Hiraishi, N., and Matsuzawa, M. (2013). Topographic precursors and geological structures of deep-seated catastrophic landslides caused by typhoon Talas. *Geomorphology*, 201:479–493.

Dade, W. B. and Huppert, H. E. (1998). Long-runout rockfalls. *Geology*, 26(9):803–806.

Ekström, G. and Stark, C. P. (2013). Simple scaling of catastrophic landslide dynamics. *Science*, 339(6126):1416–1419.

Farin, M., Mangeney, A., and Roche, O. (2014). Fundamental changes of granular flow dynamics, deposition, and erosion processes at high slope angles: insights from laboratory experiments. *Journal of Geophysical Research: Earth Surface*, 119(3):504–532.

Favreau, P., Mangeney, A., Lucas, A., Crosta, G., and Bouchut, F. (2010). Numerical modeling of landquakes. *Geophys. Res. Lett*, 37:L15305.

Fernández-Nieto, E. D., Garres-Díaz, J., Mangeney, A., and Narbona-Reina, G. (2016). A multilayer shallow model for dry granular flows with the $\mu(i)$-rheology: application to granular collapse on erodible beds. *Journal of fluid mechanics*, 798:643–681.

Geospatial Information Authority of Japan (2017). Basemap information download service.

Guthrie, R., Friele, P., Allstadt, K., Roberts, N., Evans, S., Delaney, K., Roche, D., Clague, J., and Jakob, M. (2012). The 6 August 2010 Mount Meager rock slide-debris flow, coast mountains, British Columbia: characteristics, dynamics, and implications for hazard and risk assessment. *Natural Hazards and Earth System Sciences*, 12(5):1277–1294.

Hasegawa, H. and Kanamori, H. (1987). Source mechanism of the Magnitude 7.2 Grand Banks earthquake of November 1929: Double couple or submarine landslide? *Bulletin of the Seismological Society of America*, 77(6):1984–2004.

Hibert, C., Ekström, G., and Stark, C. P. (2017). The relationship between bulk-mass momentum and short-period seismic radiation in catastrophic landslides. *Journal of Geophysical Research: Earth Surface*, 122(5):1201–1215.

Hibert, C., Stark, C., and Ekström, G. (2015). Dynamics of the Oso-steelhead landslide from broadband seismic analysis. *Natural Hazards and Earth System Sciences*, 15(6):1265–1273.

Hsü, K. J. (1975). Catastrophic debris streams (Sturzstroms) generated by rockfalls. *Geol. Soc. Am. Bull.*, 86(1):129–140.

Ionescu, I. R., Mangeney, A., Bouchut, F., and Roche, O. (2015). Viscoplastic modeling of granular column collapse with pressure-dependent rheology. *Journal of Non-Newtonian Fluid Mechanics*, 219:1–18.

Iverson, R. M. (1997). The physics of debris flows. *Reviews of geophysics*, 35(3):245–296.

Jop, P., Forterre, Y., and Pouliquen, O. (2006). A constitutive law for dense granular flows. *arXiv preprint cond-mat/0612110*.

Kawakatsu, H. (1989). Centroid single force inversion of seismic waves generated by landslides. *Journal of Geophysical Research*, 94(B9):12363–12,374.

Kuo, C., Tai, Y., Bouchut, F., Mangeney, A., Pelanti, M., Chen, R., and Chang, K. (2009). Simulation of tsaoling landslide, Taiwan, based on Saint Venant equations over general topography. *Engineering Geology*, 104(3):181–189.

Kuo, C., Tai, Y., Chen, C., Chang, K., Siau, A., Dong, J., Han, R., Shimamoto, T., and Lee, C. (2011). The landslide stage of the Hsiaolin catastrophe: Simulation and validation. *Journal of Geophysical Research*, 116(F4):F04007.

Legros, F. (2002). The mobility of long-runout landslides. *Engineering Geology*, 63(3):301–331.

Liu, W., He, S., Li, X., and Xu, Q. (2016). Two-dimensional landslide dynamic simulation based on a velocity-weakening friction law. *Landslides*, 13(5):957–965.

Lucas, A., Mangeney, A., and Ampuero, J. P. (2014). Frictional velocity-weakening in landslides on earth and on other planetary bodies. *Nature communications*, 5.

Mangeney, A., Heinrich, P., and Roche, R. (2000). Analytical solution for testing debris avalanche numerical models. *Pure and Applied Geophysics*, 157(6-8):1081–1096.

Mangeney, A., Roche, O., Hungr, O., Mangold, N., Faccanoni, G., and Lucas, A. (2010). Erosion and mobility in granular collapse over sloping beds. *Journal of Geophysical Research: Earth Surface*, 115(F3).

Mangeney-Castelnau, A., Bouchut, F., Vilotte, J., Lajeunesse, E., Aubertin, A., and Pirulli, M. (2005). On the use of Saint Venant equations to simulate the spreading of a granular mass. *Journal of Geophysical Research: Solid Earth*, 110(B9).

Moretti, L., Allstadt, K., Mangeney, A., Capdeville, Y., Stutzmann, E., and Bouchut, F. (2015). Numerical modeling of the Mount Meager landslide constrained by its force history derived from seismic data. *Journal of Geophysical Research: Solid Earth*, 120(4):2579–2599.

Moretti, L., Mangeney, A., Capdeville, Y., Stutzmann, E., Huggel, C., Schneider, D., and Bouchut, F. (2012). Numerical modeling of the Mount Steller landslide flow history and of the generated long period seismic waves. *Geophys. Res. Lett*, 39:L16402.

Nakano, M., Kumagai, H., and Inoue, H. (2008). Waveform inversion in the frequency domain for the simultaneous determination of earthquake source mechanism and moment function. *Geophysical Journal International*, 173(3):1000–1011.

Okada, Y., Kasahara, K., Hori, S., Obara, K., Sekiguchi, S., Fujiwara, H., and Yamamoto, A. (2004). Recent progress of seismic observation networks in Japan. *Earth, Planets and Space*, 56(8):xv–xxviii.

Pastor, M., Blanc, T., Haddad, B., Petrone, S., Morles, M. S., Drempetic, V., Issler, D., Crosta, G., Cascini, L., and Sorbino, G. (2014). Application of a SPH depth-integrated model to landslide run-out analysis. *Landslides*, 11(5):793–812.

Pouliquen, O. and Forterre, Y. (2002). Friction law for dense granular flows: application to the motion of a mass down a rough inclined plane. *Journal of fluid mechanics*, 453:133–151.

Public Works Research Institute, Japan (2017). List of the past deep-seated landslides.

Scheidegger, A. (1973). On the prediction of the reach and velocity of catastrophic landslides. *Rock Mechanics and Rock Engineering*, 5(4):231–236.

Schneider, D., Bartelt, P., Caplan-Auerbach, J., Christen, M., Huggel, C., and McArdell, B. W. (2010). Insights into rock-ice avalanche dynamics by combined analysis of seismic recordings and a numerical avalanche model. *Journal of Geophysical Research: Earth Surface*, 115(F4).

Schulz, W. H., McKenna, J. P., Kibler, J. D., and Biavati, G. (2009). Relations between hydrology and velocity of a continuously moving landslide – evidence of pore-pressure feedback regulating landslide motion? *Landslides*, 6(3):181–190.

Tang, C., Hu, J., Lin, M., Angelier, J., Lu, C., Chan, Y., and Chu, H. (2009). The Tsaoling landslide triggered by the Chi-Chi earthquake, Taiwan: Insights from a discrete element simulation. *Engineering Geology*, 106(1-2):1–19.

Ueno, H., Hatakeyama, S., Aketagawa, T., Funasaki, J., and Hamada, N. (2002). Improvement of hypocenter determination procedures in the Japan meteorological agency. *Quarterly Journal of Seismology*, 65:123–134.

Wessel, P. and Smith, W. (1991). Free software helps map and display data. *Eos*, 72(441):445–446.

Yamada, M., Kumagai, H., Matsushi, Y., and Matsuzawa, T. (2013). Dynamic landslide processes revealed by broadband seismic records. *Geophysical Research Letters*, 40(12):2998–3002.

Yamada, M., Mangeney, A., Matsushi, Y., and Moretti, L. (2016). Estimation of dynamic friction of the Akatani landslide from seismic waveform inversion and numerical simulation. *Geophysical Journal International*, 206(3):1479–1486.

Acknowledgements We acknowledge the National Research Institute for Earth Science and Disaster Prevention for the use of F-net and Hi-net tiltmeter data. Data are available at http://www.fnet.bosai.go.jp/top.php. High-resolution DEM data, which have been used to calculate landslide volumes, were provided by the Nara Prefectural Government and the Kinki Regional Development Bureau of the Ministry of Land, Infrastructure and Transport. This research is funded by the John Mung Program (Kyoto university young scholars overseas visit program) in 2014, the ANR contract ANR-11-BS01-0016 LANDQUAKES, CNCSUEFISCDI project PN-II-ID-PCE-2011-3-0045, the USPC PAGES project, and the ERC contract ERC-CG-2013-PE10-617472 SLIDEQUAKES. We appreciate for reviewers and Professor Jim Mori in Kyoto University providing very useful comments to improve our manuscript. We used generic mapping tools (GMT) to draw the figures (Wessel and Smith 1991).

Figures and Tables

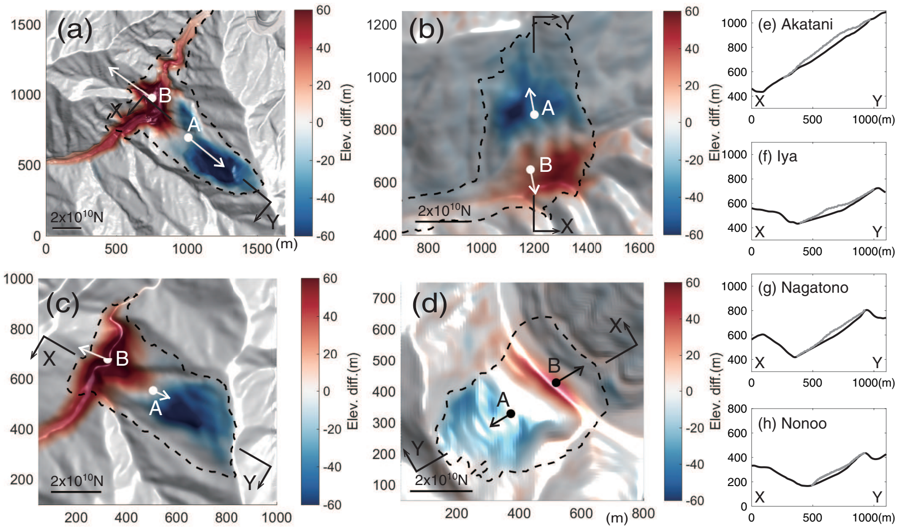

Fig. 1 Topography of (a) Akatani, (b) Iya, (c) Nagatono, and (d) Nonoo landslides and its section (e)-(h). Colors show the elevation changes at the landslide estimated from airborne LiDAR topographic surveys. Arrows show the peak of force during acceleration phase A and deceleration phase B at the center of mass. Dashed line shows the extent of the landslide excluding the landslide dam. X and Y show the line of section.

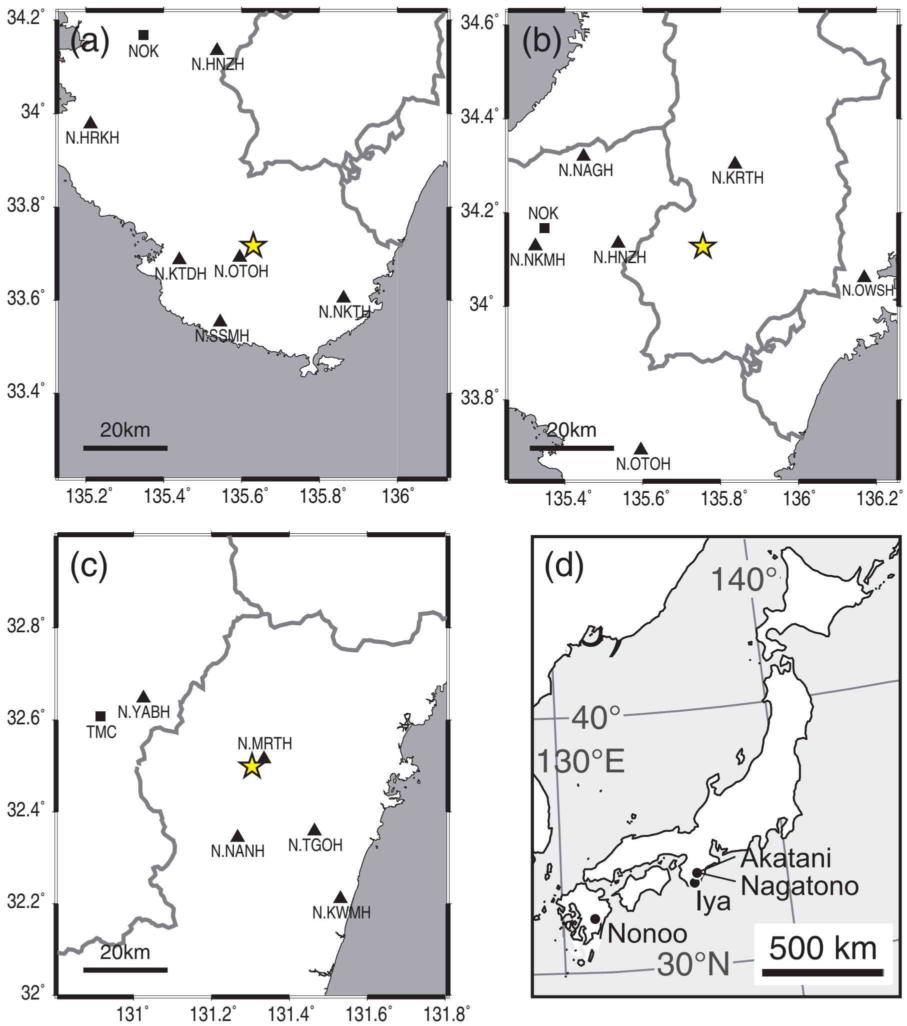

Fig. 2 Station distribution of seismic waveform inversion for (a) Iya, (b) Nagatono, and (c) Nonoo landslides. (d) Map of Japan and location of landslides. Stars show landslide location, and triangles and squares show high-sensitivity accelerograms and F-net broadband seismograms, respectively. Station distribution for Akatani landslide is shown in Yamada et al. (2013) as supporting information.

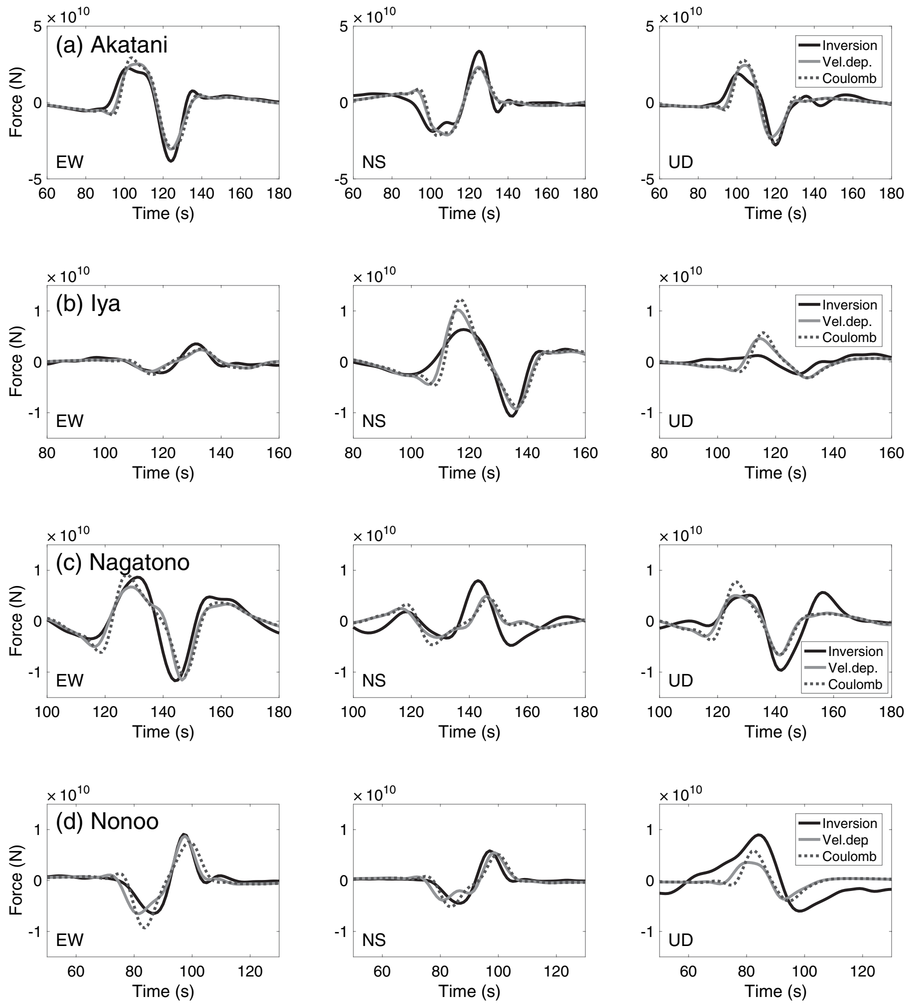

Fig. 3 Comparison between the forces obtained from seismic waveform inversion (black lines) and forces obtained from numerical simulations with velocity dependent friction model (gray solid lines) and Coulomb friction model (gray broken lines). (a) Akatani (Yamada et al. 2016), (b) Iya, (c) Nagatono, and (d) Nonoo landslides.

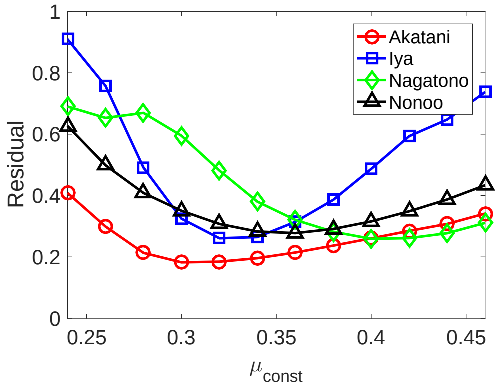

Fig. 4 Residual of the coefficients of the Coulomb friction model.

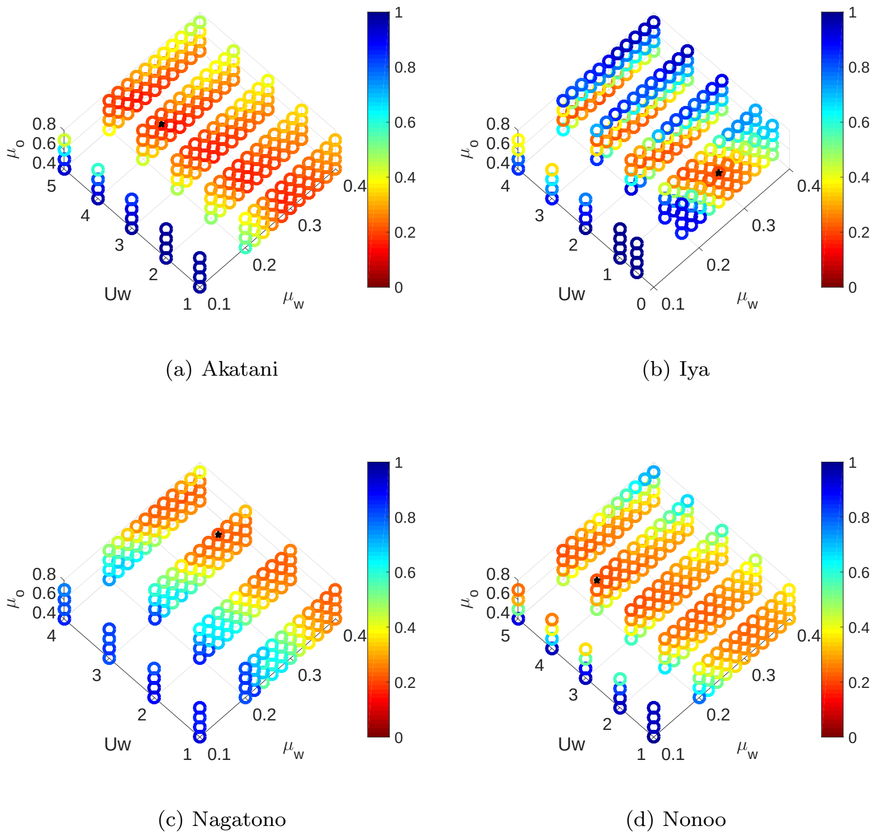

Fig. 5 Three dimensional residual space for a grid search of the velocity dependent friction model of (a) Akatani (Yamada et al. 2016), (b) Iya, (c) Nagatono, and (d) Nonoo landslides. Colors correspond to the residual values. Black stars show the minimum residual.

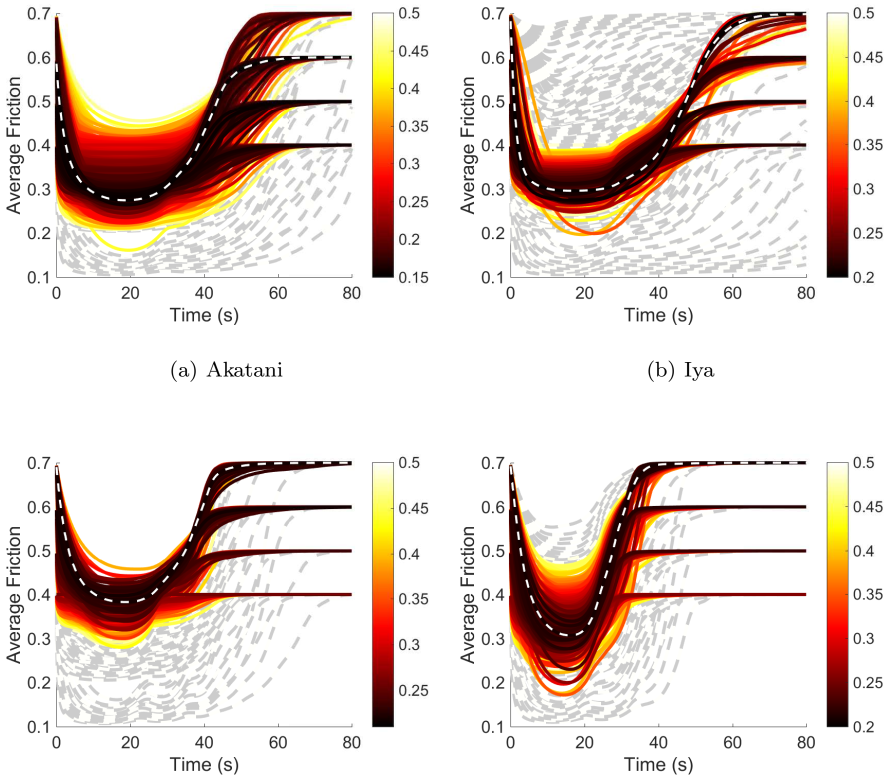

(c) Nagatono

(d) Nonoo

Fig. 6 The time history of the average coefficient of friction for each model in Figure 5. Colors indicate the residual of each model. The white dashed line shows the model with the minimum residual.

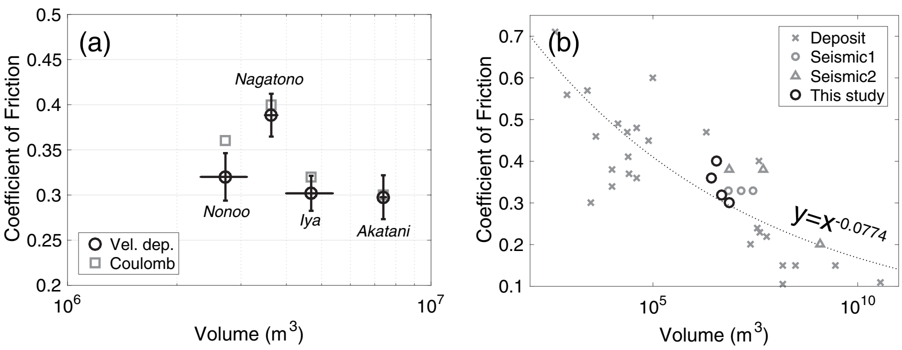

Fig. 7 Relationship between the volume of landslides and coefficient of friction during sliding. (a) The results of this study. Circles show the coefficient of friction during sliding of the velocity dependent friction model with small residuals. Gray squares show the coefficient of friction of the constant friction model. (b) Comparison with other studies. Results of the x marks are obtained by the numerical simulation benchmarked by the deposits, circles are obtained by the numerical simulation benchmarked by the seismic signals, and triangles are obtained by the force history of seismic waveform inversion.

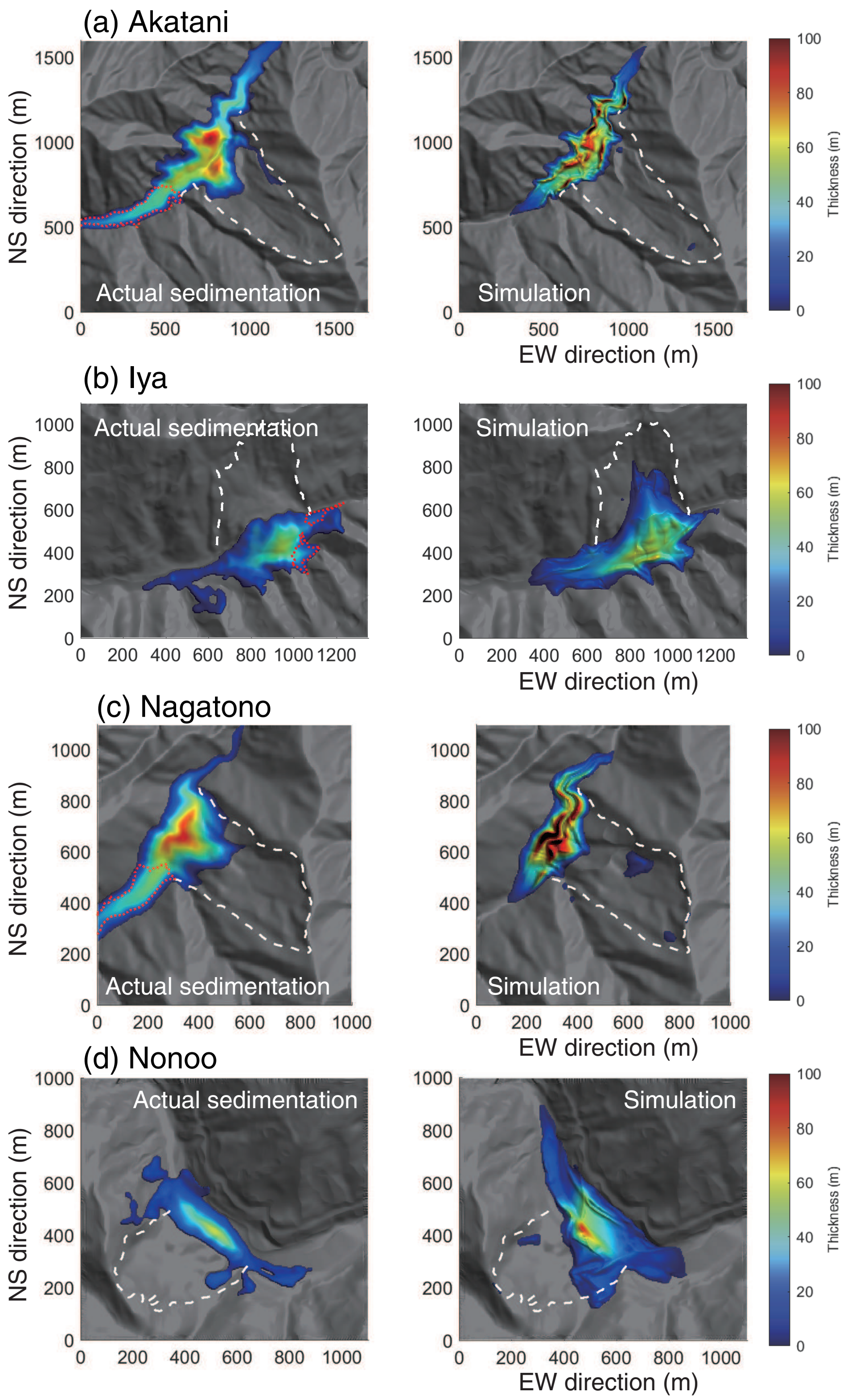

Fig. 8 Runout extent of the landslides. Left: deposit in the DEM, right: result of simulation. The white dashed line shows the extent of the landslide source and red dotted line shows the landslide dam.

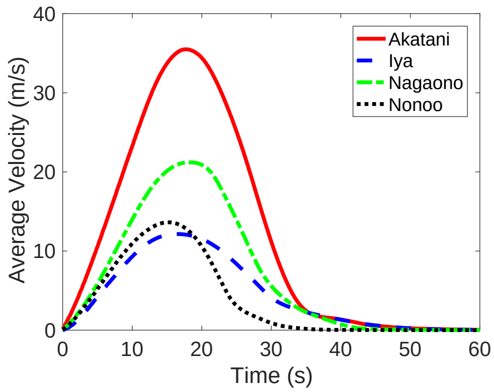

Fig. 9 Time history of the velocity at the center of mass for the most probable parameter set of the velocity dependent friction model.

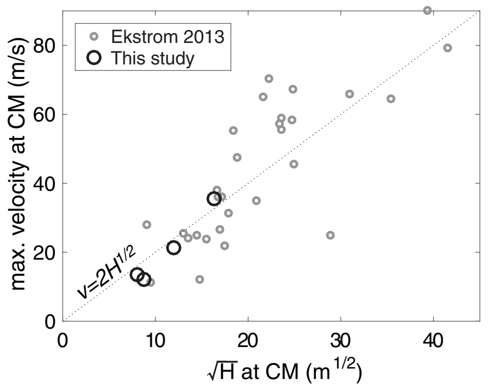

Fig. 10 Relationship between the elevation change at the center of mass before and after the landslide and maximum velocity at the center of mass. Gray circles show the results of Ekström and Stark (2013).

Supporting Information for "Estimation of dynamic friction and movement history of large landslides"

Additional Supporting Information (Files uploaded separately)

Captions for Movies S1 to S3

Introduction The supporting information contains five figures and three movies. The movies show the result of the numerical simulation.

Movie S1. The snapshots of the height of the mass of each grid for the numerical simulation of the Iya landslide with velocity dependent friction law.

Movie S2. The snapshots of the height of the mass of each grid for the numerical simulation of the Nagatono landslide with velocity dependent friction law.

Movie S3. The snapshots of the height of the mass of each grid for the numerical simulation of the Nonoo landslide with velocity dependent friction law.

Contents of this file: Figures S1 to S3

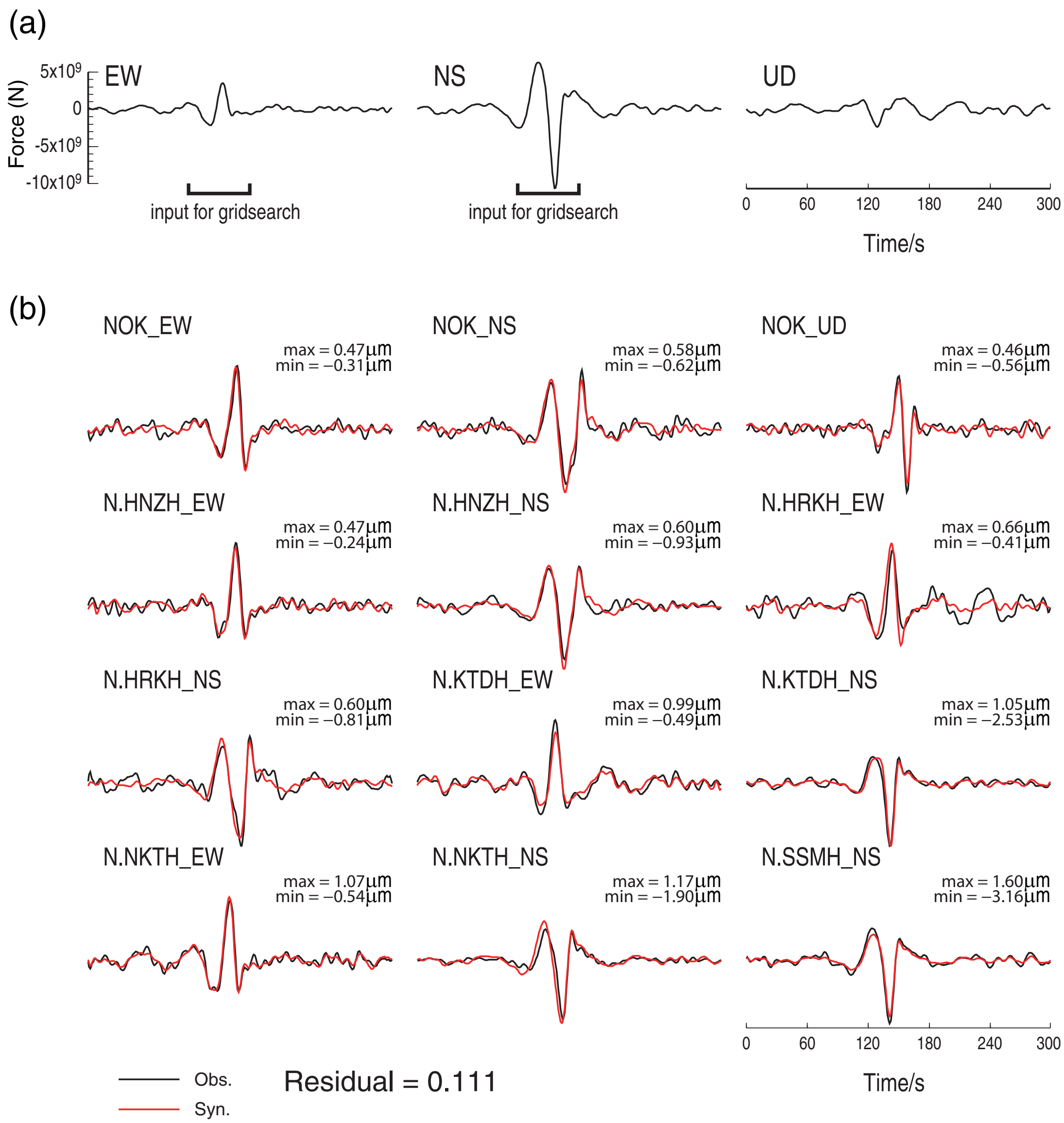

Figure S1: Seismic waveforms of the Iya landslides. (a) Estimated single-force source time functions for the EW, NS, and UD components. The windows used for a gridsearch of the best friction model is shown under the waveforms. (b) Displacement waveform fits between observed (black) and synthetic (red) data obtained from the source inversion. The letters on the left show the station code, and the numbers in the top right show the maximum and minimum amplitudes. The normalized residual of the waveform inversion is also shown at the bottom.

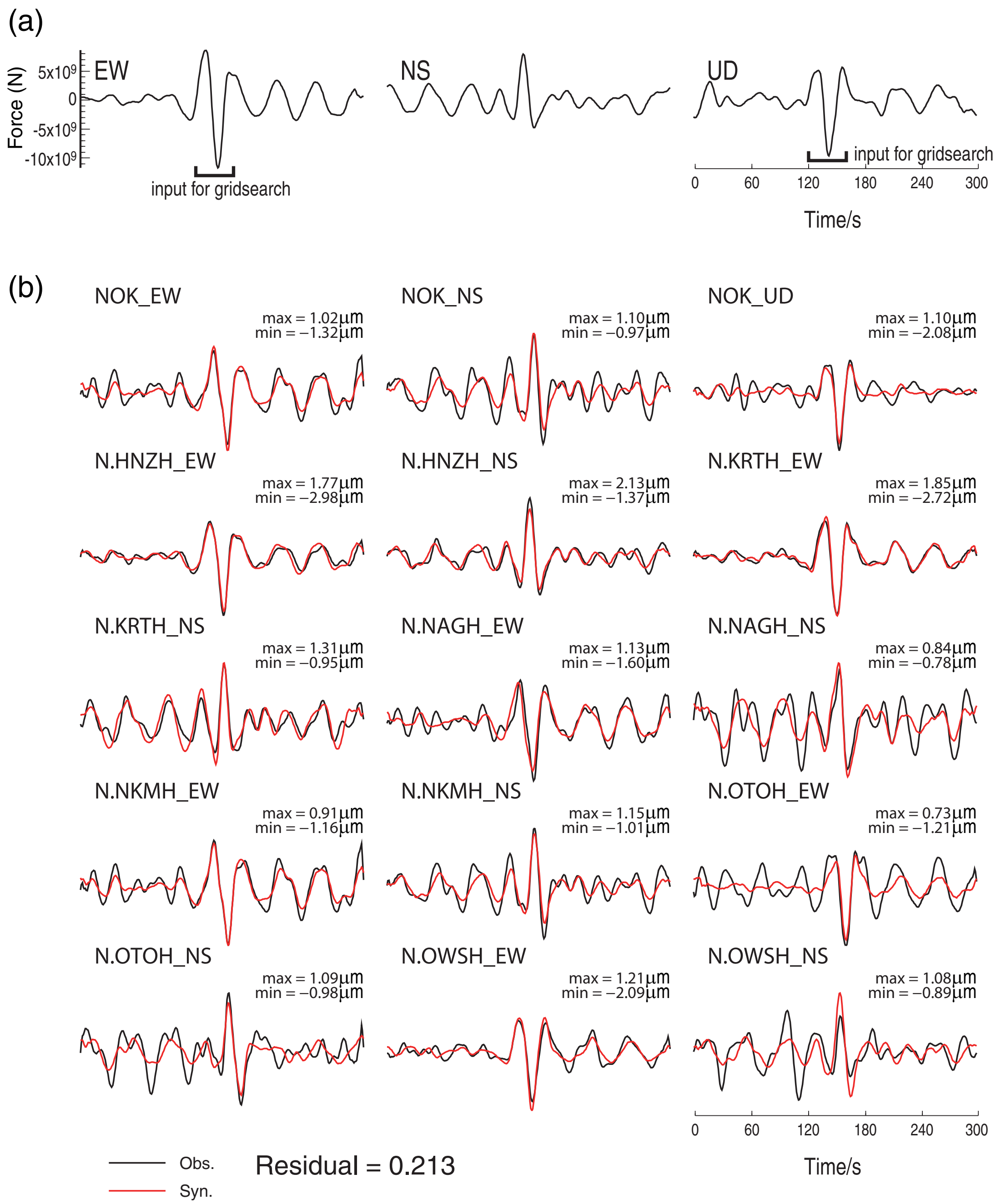

Figure S2: Seismic waveforms of the Nagatono landslides. The format is the same as Figure S1.

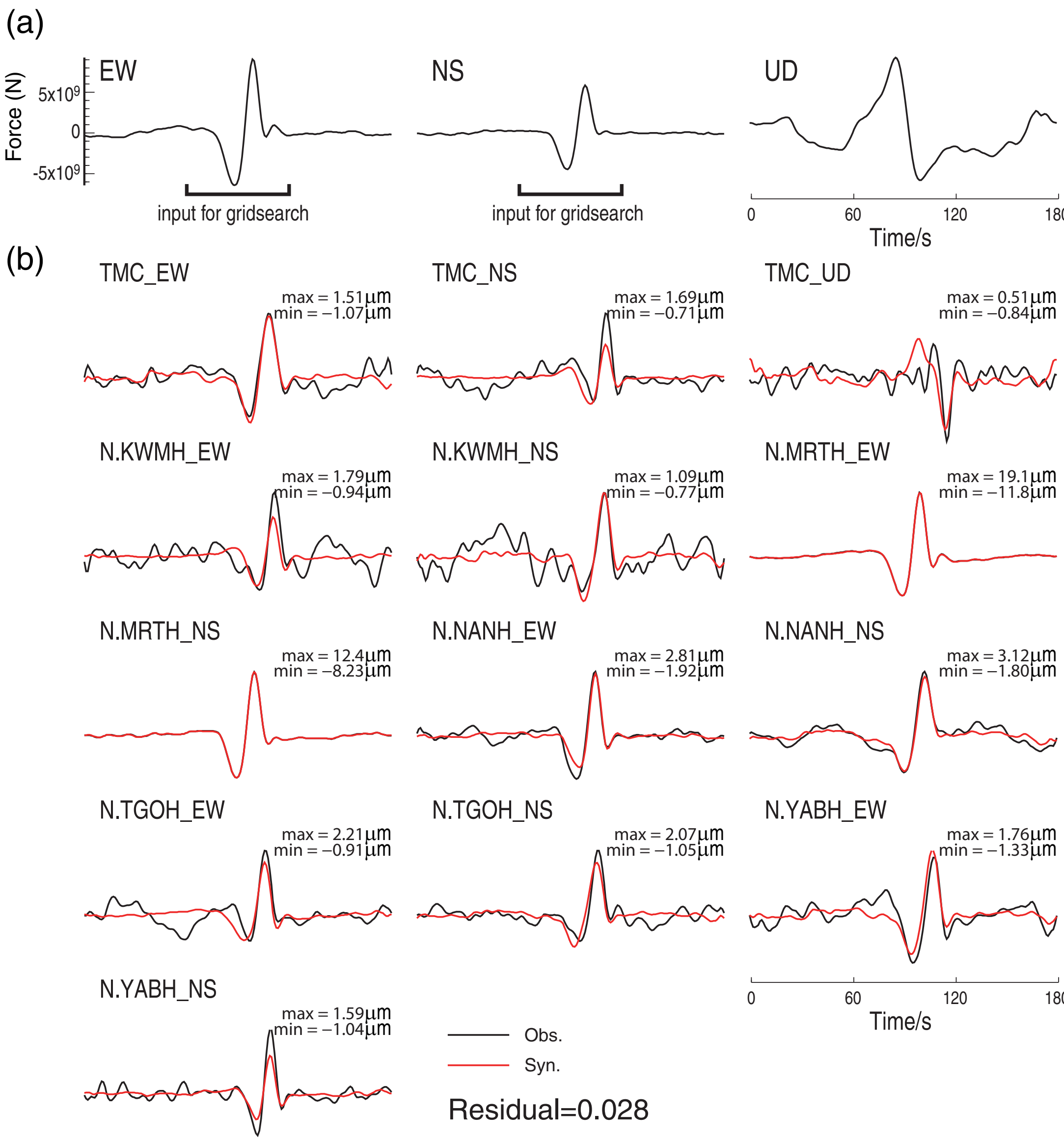

Figure S3: Seismic waveforms of the Nonoo landslides. The format is the same as Figure S1.